International Journal of MATERIALS RESEARCH

Zeitschrift für METALLKUNDE

Original Contributions

J. Su et al.: Effects of hydroxyapatite content on mechanical properties and in-vitro corrosion behavior of ZK60/HA

Jinlong Su^a, Jie Teng^a, Zili Xu^b, Yuan Li^b

^aCollege of Materials Science and Engineering, Hunan University, Changsha, P.R. China

Effects of hydroxyapatite content on mechanical properties and in-vitro corrosion behavior of ZK60/HA composites

In this study, hydroxyapatite-reinforced ZK60 Mg alloy-based composites were fabricated via a powder metallurgy route. The mechanical properties of these composites were studied by compressive tests and hardness tests. The in-vitro corrosion behavior was also investigated using immersion testing and electrochemical measurement. The influence of hydroxyapatite content on the mechanical properties and in-vitro corrosion behavior was evaluated. The microstructure and corrosion morphology were characterized by means of X-ray diffraction, optical and scanning electron microscopy. The results showed that the composite materials with 10 wt.% hydroxyapatite exhibited a better combination of mechanical strength and corrosion resistance. Compared with ZK60 alloy, the addition of 10 wt.% hydroxyapatite resulted in an increase in corrosion resistance by 38.6%.

Keywords: Magnesium matrix composite; Hydroxyapatite; Biomaterial; Mechanical properties; In-vitro corrosion

1. Introduction

Clinical orthopedic implants are usually made of titanium alloys, cobalt—chromium alloys and stainless steel. However, on the one hand, these materials cause the stress shielding effect, and on the other hand, they cannot be degraded in the human body and secondary operation for implant removal cannot be avoided, which brings the patient economic burden and physical pain, and inevitably morbid-

ity [1]. More seriously, in certain cases, orthopedic implants may be integrated with bone tissue during the healing process, which makes the retraction process difficult.

Magnesium (Mg) and its alloys have the potential to become biodegradable implants due to its biodegradability in the physiological environment and because the hydroxide products produced by degradation can be excreted by the human body [2-5]. The comparable density of Mg and its alloys (1.78- 2.0 g cm^{-3}) is similar to human bone $(1.8-2.1 \text{ g cm}^{-3})$ [6], and the elasticity modulus of Mg (about 45 GPa) is much lower than that of traditional implant materials such as stainless steel (189-205 GPa), cobalt-chromium alloys (230 GPa) and titanium alloys (105-117 GPa). The elastic modulus of human bone is about 3-20 GPa, so Mg and its alloys can effectively alleviate the stress shielding effect [1]. However, the main shortcoming of Mg and its alloys is the high corrosion rate in the physiological environment, which causes the material failure before the bone tissue is healed completely [2]. Furthermore, the rapid degradation of an Mg alloy will produce a large volume of H₂ bubbles around the implants and can lead to tissue alkalization, which slows the healing rate of the bone tissue. Therefore, it is extremely important to enhance the corrosion resistance of Mg alloy to meet the request for biomedical applications [7-9]. There mainly exist three methods of such improvement: (i) to fabricate an Mg alloy, which often lacks of excellent biocompatibility; (ii) to prepare a coating by complex chemical processes on Mg alloys' surface, which often leads to high cost and pollution; (iii) to fabricate Mg-based composites reinforced with bioceramics such as hydroxyapa-

^bThe first affiliated hospital, Hunan Normal University, Changsha, P.R. China

tite (HA) and tricalcium phosphate (TCP), which is considered a promising method to meet the clinical requirement for high corrosion resistance and excellent biocompatibility [10].

Sunil et al. [11] fabricated Mg/xHA (x = 0, 5, 10 and 15 wt.%) composites via ball milling and spark plasma sintering, and studied the corrosion properties of these composites. The results showed that Mg/10HA composite had the best corrosion resistance because of lower inter-lamellar corrosion and higher resistance to localized pitting. Campo et al. [12] prepared Mg/xHA (x = 0, 5, 10 and 15 wt.%) composites by a powder metallurgy method, and pointed out that pure Mg exhibited a five times higher corrosion penetration rate than Mg/5HA composite after immersion in PBS solution for 100 h. Witte et al. [13] fabricated AZ91D/20HA composite by a powder metallurgy route and investigated its corrosion behavior. However, it is reported that Al is harmful to the nervous system, and consequently AZ91D/20HA composite is unsuitable for orthopedic application [14, 15]. Feng and Han [16] fabricated ZK60A matrix composites reinforced with various amounts of calcium polyphosphate (CPP) (0, 2.5, 5, 7.5 and 10 wt.%) particles through powder metallurgy and studied CPP's effects on the corrosion behavior. The results indicated that increasing HA content was beneficial to the improvement of corrosion resistance while the agglomeration of CPP particles occurred when the content of CPP was more than 7.5 wt.%. In another study, Mg-Zn-Zr alloy based composite reinforced with 1 wt.% nano-HA particles was fabricated and exhibited better corrosion resistance and biocompatibility than Mg-Zn-Zr alloy [17]. In addition, Shuai et al. [18] fabricated Mg-3Zn/xHA (x = 0, 2.5, 5, 7.5 and 10 wt.%) via selective laser melting, and they found that with increasing HA content, the grain size of Mg-3Zn/HA composites decreased gradually, while the hardness and corrosion resistance was increased.

ZK60 Mg alloy is a promising material for biomedical application; it is composed of Mg, Zn and Zr. Zn is an essential trace element in the human body, and Mg-Zn binary alloys exhibit great biocompatibility [19, 20]. Cai et al. [21] prepared Mg-xZn alloys (x = 1, 5 and 7 wt.%) through a melting process, and the result indicate that Mg-5Zn exhibit the best mechanical properties and corrosion resistance. In previous studies, Zr has been adopted in biocompatible Ti alloys [22]. In the Mg-Zr binary alloy system, Zr can effectively improve the corrosion resistance of materials when the content of Zr is less than 0.48 % with no formation of insoluble Zr particles in Mg [23]. The enhancement of mechanical properties and corrosion resistance can be achieved by the addition of Zr into Mg-Zn alloy [24]. Hydroxyapatite (Ca₁₀(PO₄)₆(OH)₂, HA), as a component of natural bone, exhibits excellent biocompatibility and low solubility in body [25]. HA is suitable as reinforcement in Mg alloys as it can enhance corrosion performance of the composites through inducing the apatite formation [26, 27]. At present, however, the overall performance of the Mg-Zn-Zr alloy reinforced with a wide range of HA content have not been reported.

In this work, ZK60/xHA composites (x = 0, 5, 10, 15 and 20 wt.%) were fabricated by a powder metallurgy method. X-ray diffraction (XRD), optical microscopy (OM) and scanning electron microscopy (SEM) were used to characterize the microstructure of these composites. Mechanical properties were also studied by hardness tests and compressive tests, and in-vitro corrosion behavior of the composites in simulated body fluid (SBF) solution was investigated by immersion test and electrochemical measurement.

2. Experimental procedure

2.1. Materials preparation

ZK60/HA composites reinforced with 5, 10, 15 and 20 wt.% of HA were prepared via powder metallurgy. Gas-atomized ZK60 alloy powders (Zn 5.1 wt.%, Zr 0.18 wt.%, 30–50 μm, Tangshan Weihao Magnesium Powder Co., Ltd., China) and hydroxyapatite powders (2–10 μm, Beijing DK Nanotechnology Co., LTD., China) were selected as matrix alloy powder and reinforcement, respectively. First, the ZK60 alloy powders were mechanically milled for 1.5 h at 400 rpm with a planetary ball mill to remove the surface oxide film. Then, the ZK60 and HA powders were mixed evenly through ball milling in an agate tank. The rotation speed was 200 rpm, and the ball milling was performed for 30 mins including a forward rotation of 15 mins and a reverse rotation of 15 mins. The mixed powders were placed in a mold with a vacuum environment of 5 Pa, and were heated to 180 °C and pre-compacted at a force of 100 MPa to obtain a powder ingot billet. Then, the billet was subjected to a further hot compression at a force of 500 MPa for 10 mins at 300 °C, and then extruded with an extrusion ratio of 20. A bar with 10 mm diameter was obtained after extrusion. In addition, a bar of ZK60 alloy was also produced by the same process for comparison.

The samples for compressive testing (\oslash 9.1 × 15 mm), immersion test (\oslash 10 × 4.5 mm) and electrochemical measurement (\oslash 10 × 4.5 mm) were cut from the as-extruded bars using electrical discharge machining (EDM). Prior to any of the tests, all specimens were prepared by grinding with up to 2000 grit silicate paper and polishing with 1.5 μ m diamond polishing paste, followed by ultrasonic cleaning in ethanol for 5 mins.

2.2. Characterization of the composites

The density of ZK60/HA composites was measured according to the Archimedes' principle. The microstructure was examined using OM (4XCE, Shanghai Caikang Optical Instruments Co., Ltd., China), and the fracture surfaces of the composites and the morphology of corrosion specimens were characterized using SEM (EVO MA10, Carl Zeiss, Germany) and XRD (SmartLab, Rigaku Corporation, Japan) with Cu-K $_{\alpha}$ radiation (λ = 1.5418 Å).

2.3. Hardness testing

The Vickers microhardness was measured on a microhardness instrument (HVS-1000, Shanghai Caikang Optical Instruments Co., Ltd., China) along transverse directions with a load of 1 N holding for 15 s. Each sample was tested at least six times and the mean value was taken as the hardness value.

2.4. Compressive testin

The tests were conducted on a compression test machine (3382, Instron, America) at a stress increase rate of 1 N \cdot mm⁻² s⁻¹, and for each kind of the composite materials at least three samples were tested to ensure reproducibility.

2.5. Immersion testing

The solution used in the immersion test was SBF, and the ion concentration of the solution is listed in the Table 1. The preparation procedure of SBF solution was determined according to the study by Kokubo and Takadama [28].

The corrosion sample was cylindrical with \emptyset 10 × 4.5 mm, and the ratio of the surface area of immersed sample to the volume of solution was 1 cm²: 40 mL. During the experiments, the temperature of the solution was kept to 37 ± 0.5 °C by a

Table 1. Ion concentration of SBF.

Ion	Ion concentrations (mM)		
	Blood plasma	SBF	
Na ⁺	142.0	142.0	
K ⁺	5.0	5.0	
Mg ²⁺ Ca ²⁺	1.5	1.5	
Ca ²⁺	2.5	2.5	
Cl-	103.0	147.8	
HCO ³⁻	27	4.2	
HPO ^{4–}	1.0	1.0	
SO4 ²⁻	0.5	0.5	
pН	7.2–7.4	7.40	

thermostatic water bath without refreshing the solutions. The hydrogen gas was collected by a filter funnel into a burette. After immersing in SBF for 10 days, each sample was taken out and ultrasonically cleaned in a chromic acid solution (200 g L⁻¹ CrO₃ + 10 g L⁻¹ AgNO₃) for 5 mins to remove corrosion products on the surface, followed by further washing with distilled water and ultrasonic cleaning in ethanol for 3 mins. Then, the samples were weighed to calculate the mass loss. In previous studies, it has been demonstrated that the chromic acid almost has no effect on the weight loss of Mg [29]. Therefore, the difference between the original weight and the final weight is used to indicate the mass of loss in SBF.

The corrosion rate was calculated as follows:

Corrosion rate
$$(mm \ y^{-1}) = (K \times W)/(A \times T \times D)$$
 (1)

where K is a constant (8.76×10^4) , W is the mass of loss (g), A is the surface area (cm²) of the corrosion sample, T is the immersion time (h), D is the density (g cm⁻³).

After removing corrosion products, the sample was cut into two halves using EDM along the radial direction. The cut sample was mounted in resin, ground and polished for cross-sectional examination.

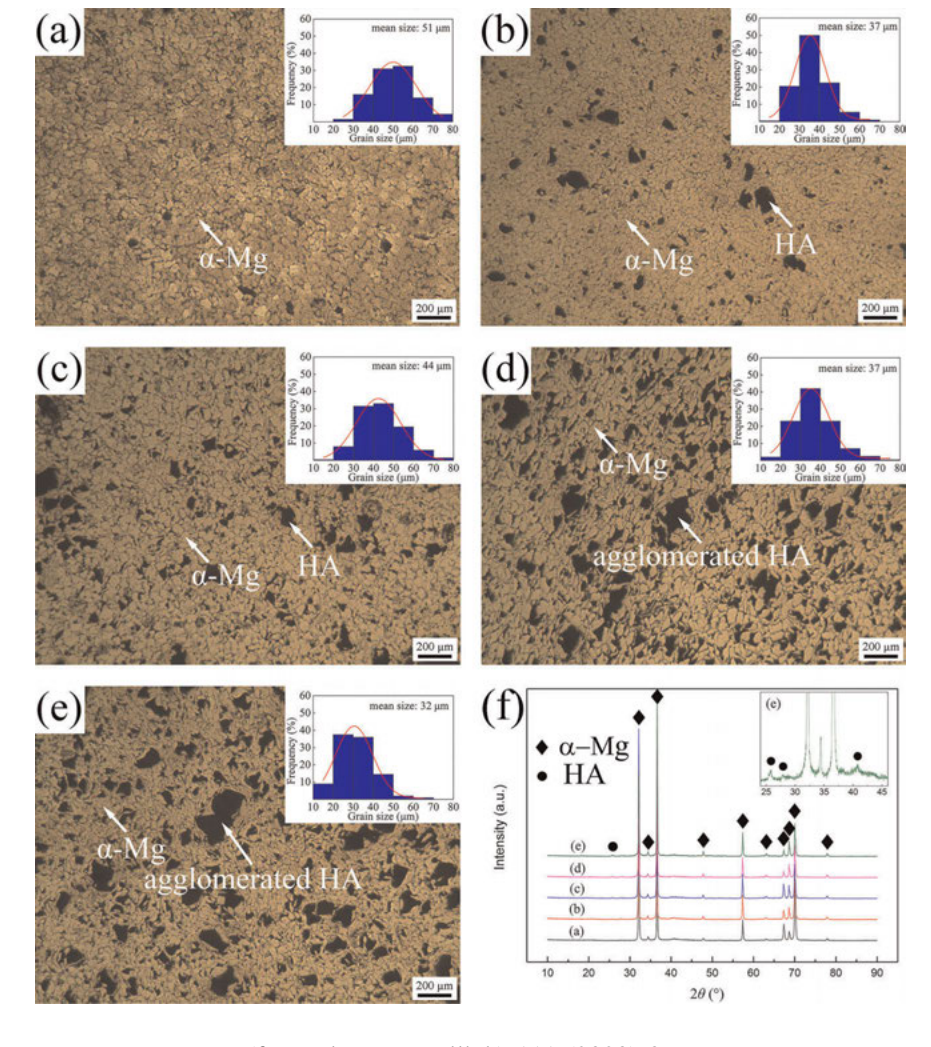


Fig. 1. Transverse-section OM images of (a) ZK60; (b) ZK60/5HA; (c) ZK60/10HA; (d) ZK60/15HA; (e) ZK60/20HA, and (f) the corresponding XRD patterns (the bright area is α-Mg, the black area is HA particles, and agglomerated HA particles can be found in ZK60/15HA and ZK60/20HA).

2.6. Electrochemical measurement

The testing was performed on an electrochemical workstation (CHI-660C, CH Instruments Inc., China). ZK60 alloy and ZK60/HA composites were selected as the working electrode. A platinum electrode and a saturated calomel electrode were used as an auxiliary electrode and a reference electrode, respectively. The working electrode was sealed in epoxy resin with an exposed geometric area of 0.78 cm². The electrolyte was SBF solution with a volume of 200 mL. Before measurements were taken, the open circuit potential (OCP) was tested until it stabilized. The scanning potential range was $OCP \pm 200$ mV, and the scanning rate was 1 mV s⁻¹.

3. Results and discussion

3.1. Characterization of the extruded samples

OM images of transverse section of ZK60 alloy and ZK60/HA composites are presented in Fig. 1. It can be found in Fig. 1a that the average grain size of ZK60 alloy was about 51 μ m. However, the average grain size of ZK60/5HA composite was about 37 μ m, which was about 27% smaller than that of ZK60 alloy, as shown in Fig. 1b. Further, as shown in Fig. 1c–e, the average grain size of ZK60/10HA, ZK60/15HA and ZK60/20HA composites was 44, 37 and 32 μ m, respectively. It becomes obvious that the addition of HA refines the grains of ZK60/HA composites. This can be attributed to the large stress concentration inside the grain during extrusion process and the effect of inhibit-

ing the grain growth due to the addition of HA particles. In addition, HA particles agglomerated to some extent as its content increased, the average size of HA particles was 12.47, 14.89, 22.92, 24.21 μ m for ZK60/5HA, ZK60/10HA, ZK60/15HA, ZK60/20HA, respectively.

As shown in Fig. 1f, the XRD patterns of ZK60 alloy and ZK60/HA composites indicated that the two phases observed were mainly $\alpha\textsc{-Mg}$ and HA. The typical intermetallic MgZn2 phase was not detected by XRD analysis of the composite materials, which could be attributed to the rapid cooling effect caused by gas atomization of alloy matrix powders when Zn has dissolved in Mg to form a supersaturated solid solution. In the subsequent powder metallurgy processing, the MgZn2 phase did not precipitate, so it could not be detected.

SEM images of the transverse section of ZK60/HA composites are shown in Fig. 2. Obviously, the interface between HA and Mg matrix was direct contact and there were almost no obvious voids when the HA content was lower than 10 wt.% (as shown in Fig. 2a and b). However, it is clear from Fig. 2c and d that when the HA content reached and exceeded 15 wt.%, voids occurred along the interface between large agglomerated HA particles and the matrix. Meanwhile, cracks also appeared inside some HA particles, as shown in the higher magnification image inserted in Fig. 2d. This may be due to strong triaxial compressive stress generated during extrusion and low ductility of HA.

The densities of ZK60 alloy and ZK60/HA composites are listed in Table 2. It can be seen that all ratios of ρ_e (experimental density) to ρ_t (theoretical density) were higher

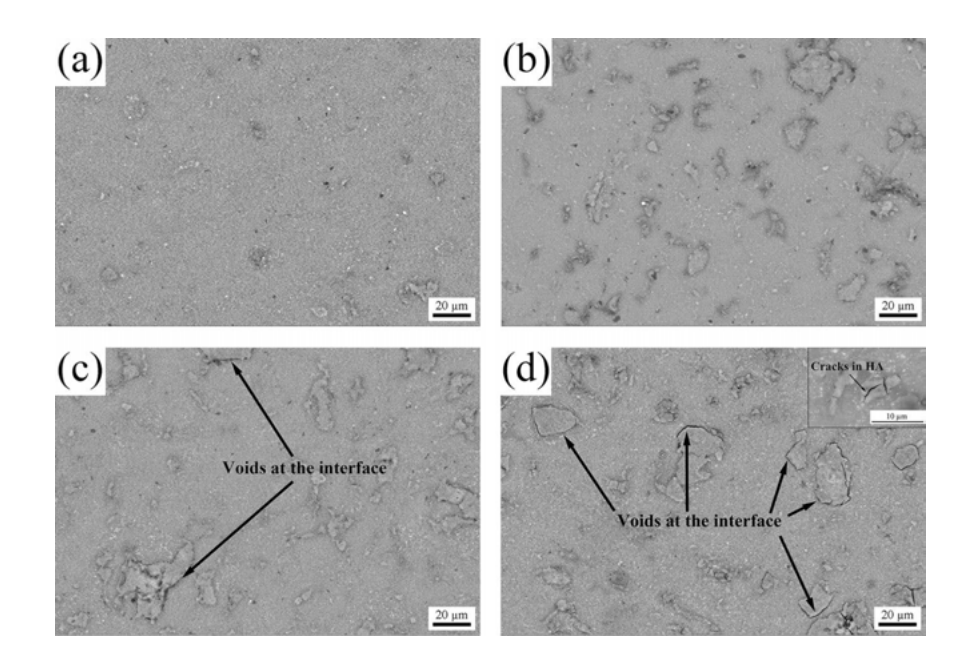


Fig. 2. Transverse-section SEM images of (a) ZK60/5HA, (b) ZK60/10HA, (c) ZK60/15HA and (d) ZK60/20HA (arrows points to the voids at the α-Mg/HA interface within ZK60/15HA and ZK60/20HA, and cracks in HA can be found in ZK60/20HA).

Table 2. ρ_e and ρ_t values of ZK60 alloy and ZK60/HA composites.

Sample	$\rho_{\rm e}({\rm g~cm^{-3}})$	$\rho_{\rm t}$ (g cm ⁻³)	$\rho_{\rm e}/\rho_{\rm t}$ (%)
ZK60	1.807	1.812	99.7
ZK60/5HA	1.812	1.852	97.8
ZK60/10HA	1.841	1.893	97.3
ZK60/15HA	1.847	1.936	95.4
ZK60/20HA	1.869	1.981	94.3

than 94%, and the relative density decreased as the content of HA increased. This also reflected the fact that the addition of HA led to voids inside the material, which was in accord with the phenomenon observed in SEM.

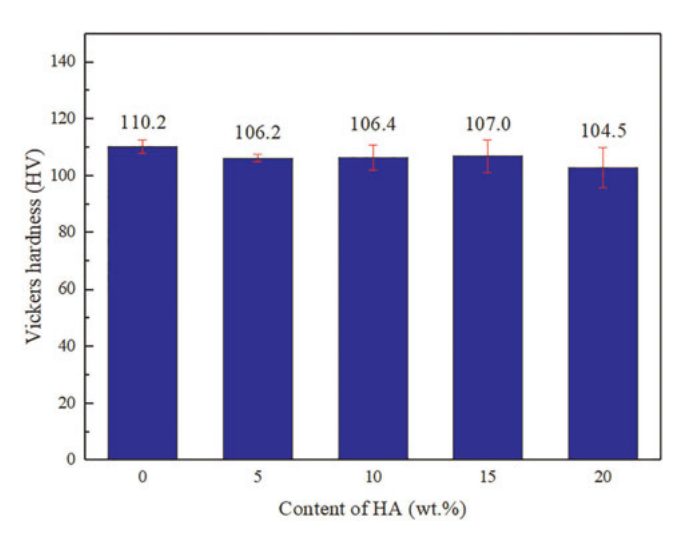


Fig. 3. Transverse-sectional Vickers micro-hardness of ZK60 alloy and ZK60/HA composites.

3.2. Hardness testing

Figure 3 shows the transverse-sectional Vickers microhardness of ZK60 alloy and ZK60/HA composites. Compared with the ZK60 alloy, the hardness of ZK60/HA composites showed a slight decrease and was also affected by the content of HA. With incorporation of 5 wt.% HA, the hardness of the composites decreased by approximate 3.6%. If the content of HA further increased to 20 wt.%, the hardness decreased by about 5.2%. Furthermore, with the increase of HA content, the hardness value of the composites showed a wider range of fluctuations, which indicated the inhomogeneity due to the agglomeration of HA particles.

3.3. Compression testing

Typical compression curves from the compressive tests are shown in Fig. 4a. Table 3 lists yield strength, ultimate compressive strength and failure strain of ZK60 alloy and ZK60/HA composites. Obviously, with an addition of 5 wt.% HA, the yield strength of the composites was increased by 17% over the ZK60 alloy. This can be attributed to homogeneous distribution of HA particles in the matrix, which offered a pinning effect. As the content of HA increased further, the yield strength and the ultimate compressive strength tended to decrease, which can be ascribed to the agglomeration of HA particles, which led to less uniform dispersion. Based on previous research, the compres-

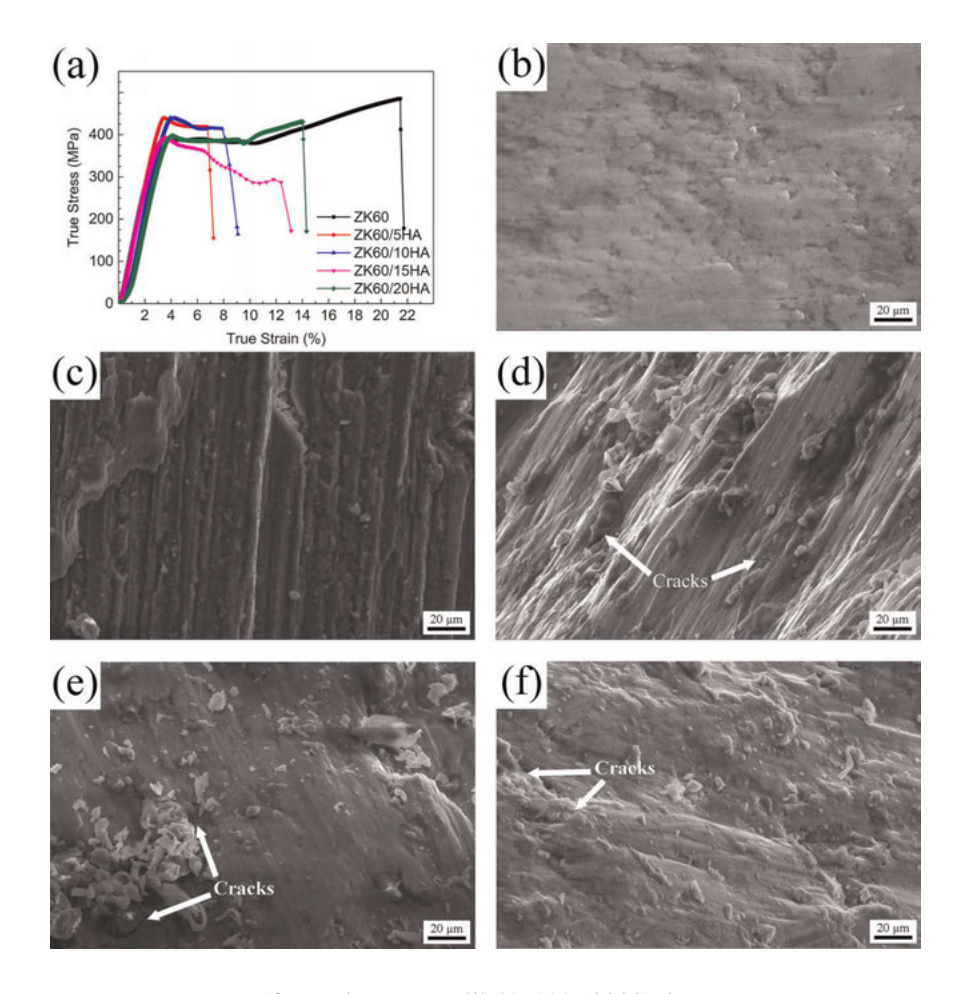


Fig. 4. (a) Typical compression curves of ZK60 alloy and ZK60/HA composites; SEM images of the compressive fracture surface of (b) ZK60, (c) ZK60/5HA, (d) ZK60/10HA, (e) ZK60/15HA and (f) ZK60/20HA.

sive yield strength of natural bone is 130–180 MPa [30]. Although the compressive strength of the composite materials decreased with the addition of HA, the strength was still higher than that of natural bone in the human body.

SEM images of the compressive fracture surfaces of ZK60 alloy and ZK60/HA composites are presented in Fig. 4b–f. It can be seen that the main feature of the fracture surfaces was the occurrence of cleavage facets and steps, and the fracture morphology of samples became rougher with the increase in HA content. Moreover, it can be seen from Fig. 4d–f that there existed agglomerated and broken HA particles on the fracture surfaces, which provided conditions for the formation and expansion of cracks.

3.4. Immersion testing

The corrosion resistance of ZK60 alloy and ZK60/HA composites in SBF can be evaluated by immersion testing. In the early stage, both ZK60 alloy and ZK60/HA composites will undergo the following chemical reaction:

$$Mg + 2H_2O \rightarrow Mg(OH)_2 + H_2 \tag{2}$$

The corrosion products of $Mg(OH)_2$ usually covered the surface of the materials and can provide some protective effect. However, $Mg(OH)_2$ is readily transformed to $MgCl_2$ when the Cl^- concentration in the aqueous solution is above 30 mmol L^{-1} [31]. Since $MgCl_2$ is soluble in aqueous solution, it does not effectively protect the matrix.

However, for ZK60/HA composites, HA has the ability to induce the formation of bonelike apatite in SBF solution by interacting between the negative charge of HA surface and the positive calcium ions in the solution, and thereby forming a Ca-rich amorphous calcium phosphate (ACP). The Ca-rich ACP has positive charge and can interact with the negative phosphate ion to form Ca-poor ACP, which finally crystallizes into the bone-like apatite [18, 27]. The apatite formed on the surface can protect the substrate well, which improves the corrosion resistance of the materials in a certain sense [26].

Figure 5a shows the released hydrogen volume of the samples as a function of time. According to Eq. (2), 1 mol Mg can produce 1 mol H_2 , so released hydrogen volume can be used to assess the corrosion rate of the materials. It can be seen that among these samples, ZK60 alloy exhibited the highest rate of released hydrogen volume while ZK60/10HA composite had the lowest rate. The released hydrogen volumes of ZK60 alloy and ZK60/10HA composite were 24.9 mL cm⁻² and 15.3 mL cm⁻², respectively. The released hydrogen volume of ZK60/10HA was 38.6 % lower than that of ZK60 alloy. According to the hydrogen evolution test, the corrosion resistance of these samples can be ranked as ZK60/10HA > ZK60/15HA > ZK60/20HA > ZK60/20HA > ZK60.

Figure 5b shows the average corrosion rate calculated on the basis of mass loss after 10 days' immersion. It is obvious that ZK60/HA composite showed better corrosion resistance

Table 3.	Yield strength,	ultimate compressive	strength and failur	e strain of ZK60 alloy	, ZK60/HA compos	sites and natural bone.

Sample	Yield strength (0.2% offset, MPa)	Ultimate compressive strength (MPa)	Failure strain (%)
ZK60	356	554	16.4
ZK60/5HA	418	459	7.8
ZK60/10HA	328	465	10.6
ZK60/15HA	334	404	12.5
ZK60/20HA	322	418	13.4
Natural bone*	130–180	-	_

^{*} Mechanical properties of natural bone were obtained from Ref. [30].

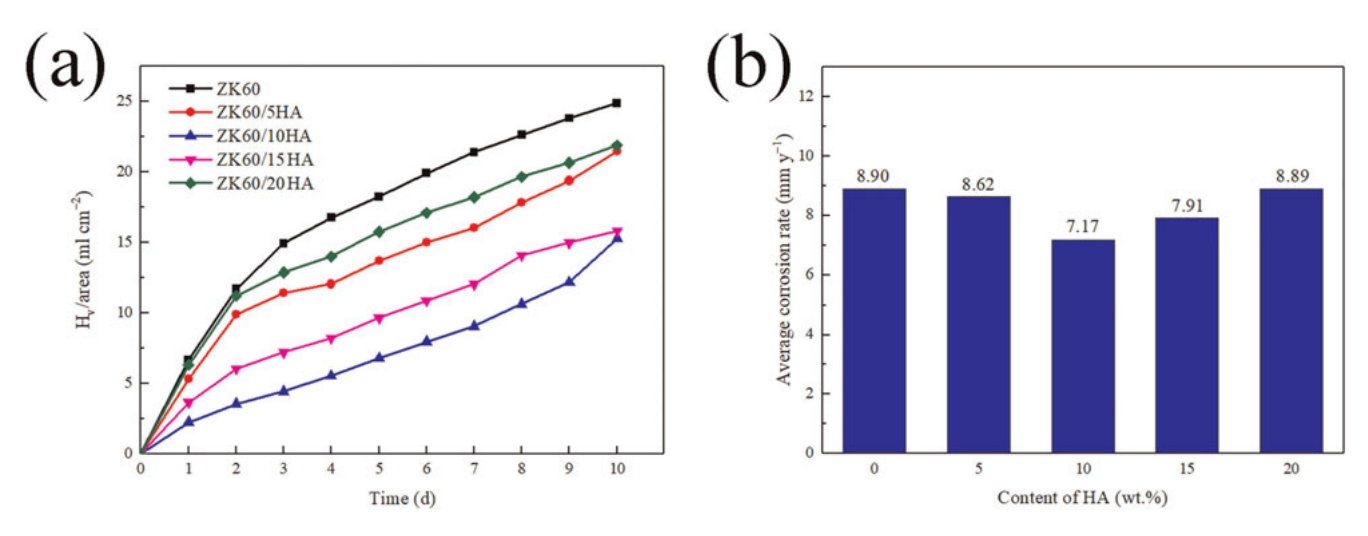
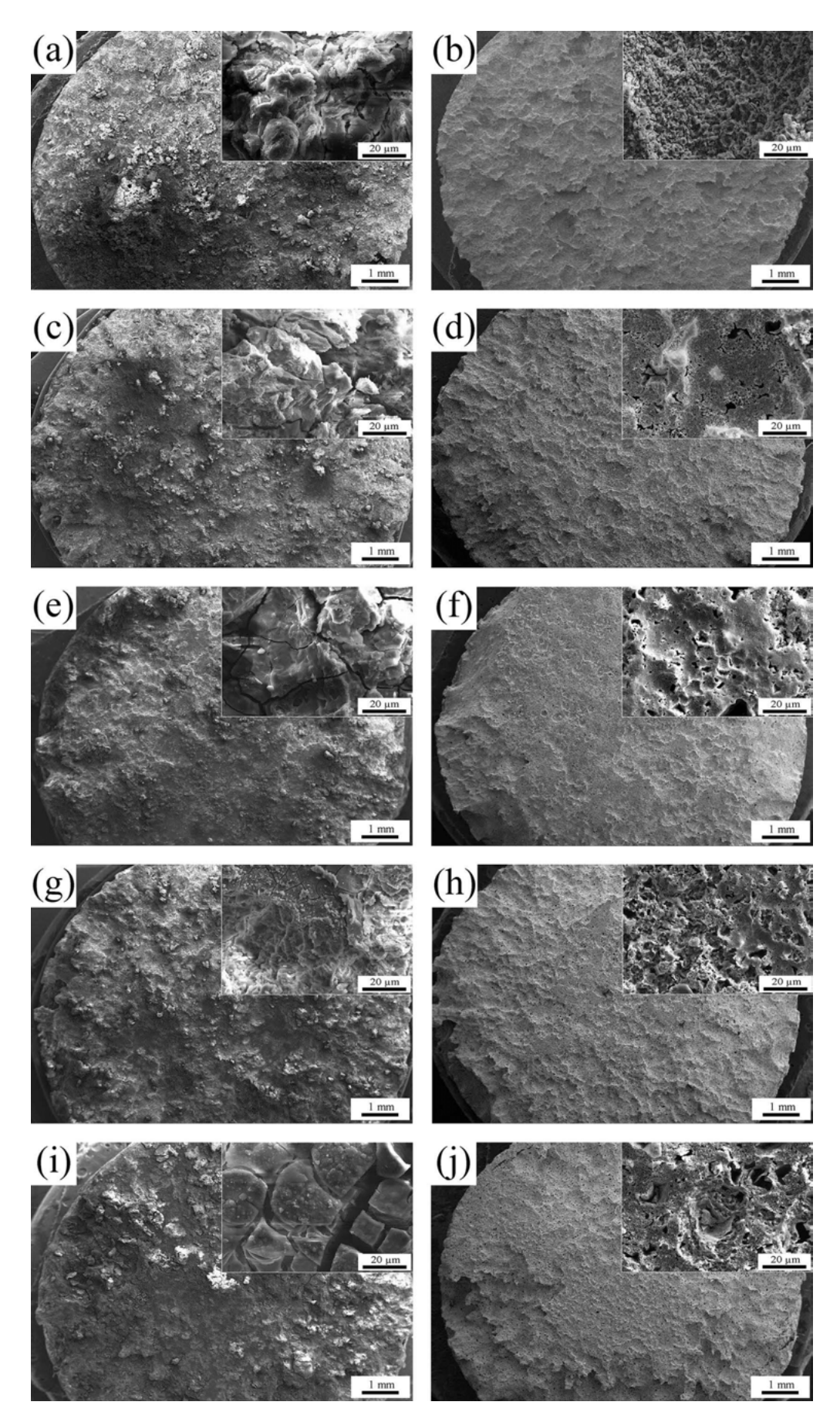


Fig. 5. (a) Released hydrogen volume divided by surface area of immersed samples as a function of time; and (b) average corrosion rate after immersion in SBF for 10 days.



 $Fig. \ 6. \ SEM \ images \ of the samples \ after \ immersion \ in \ SBF \ solution \ for \ 10 \ days \ and \ the \ corresponding \ samples \ after \ removing \ the \ corresponding \ samples \ samples$

than ZK60 alloy. The increase in corrosion resistance can be attributed to HA particles which are more resistant to corrosion by Cl- than Mg matrix. More importantly, HA can promote the formation of apatite, thereby reducing degradation rate [26]. Particularly, ZK60/10HA composite showed the minimum mass loss of 7.17 mm y⁻¹, which was 19.4% lower than 8.9 mm y⁻¹ of ZK60 alloy. The difference between the hydrogen evolution test and mass loss test was mainly attributed to the fall off of HA particles during the removal of the corrosion products in the mass loss test. So, the hydrogen evolution test can better reflect the corrosion resistance of these materials. It should be noted that when the HA content reached and exceeded 15%, the corrosion resistance of the composites was weakened. During the immersion test, the interface bonding between HA particle and the matrix was weakened, which made the HA particles easier to peel off and impeded the effect of HA on the inducing the deposition of apatite. According to the mass loss test, the corrosion resistance of materials can be ranked as ZK60/10HA > ZK60/ 15HA > ZK60/5HA > ZK60/20HA > ZK60. This is completely in agreement with the result of hydrogen evolution test.

Figure 6a, c, e, g and i presents SEM images of the samples after immersion in SBF solution for 10 days. It is obvious that a large amount of corrosion products were formed and covered the surface of the samples. As shown in the inserted images with larger magnification, the corrosion product on the surface of ZK60/HA composites was more compact than that of ZK60 alloy. Many cracks were formed on the surface of the corrosion product, which can be attributed to the dehydration of Mg(OH)₂ to MgO during the drying process. It was worth noting that the cracks of the corrosion product layer of ZK60/20HA composite were clearly wider than those of other materials (as shown in Fig. 6e. It can be assumed that these wider cracks were not only formed during the drying process,

but also can be ascribed to the more serious agglomeration of HA particles in the composites. The agglomeration resulted in many defects at the interface between HA particles and Mg matrix, and the SBF solution can readily penetrate into the matrix along the interface, thereby making the composites' interface enlarged and further corroded [18]. It can be predicted that the denser the corrosion product layer, the better the protection of the matrix. This was in agreement with the results of the hydrogen evolution test and mass loss test.

Figure 6b, d, f, h and j shows the SEM images of the corresponding samples after removing the corrosion products. In particular, as shown in the inserted images with higher magnification, the corrosion morphology of ZK60 alloy is obviously different from that of ZK60/HA composites. It can be seen from Fig. 6f that many deep pits and holes formed, which indicated serious local corrosion caused by the corrosion of Cl⁻. Compared with ZK60 alloy, ZK60/ HA composites, especially ZK60/10HA, exhibited a relatively flat surface, which represent a higher resistance to localized pitting. Moreover, some obvious holes can be found on the surface, which can be attributed to the peeling off of HA particles during the process of removing the corrosion products. Owing to the interfacial bonding between HA particle and the matrix being weakened during the immersion test, the HA particles were more easily peeled off during the process of removing the corrosion products.

Figure 7a and b presents SEM images and EDS spectra of the corroded surfaces of ZK60 alloy and ZK60/10HA composite after immersion in SBF solution for 10 days. EDS analysis was performed on the rectangular regions shown in Fig. 7a and b. It can be seen that a layer of corrosion products was formed during the corrosion process. The EDS results show that the main elements present in the corroded surface layer of ZK60 alloy were Mg and O, which represent

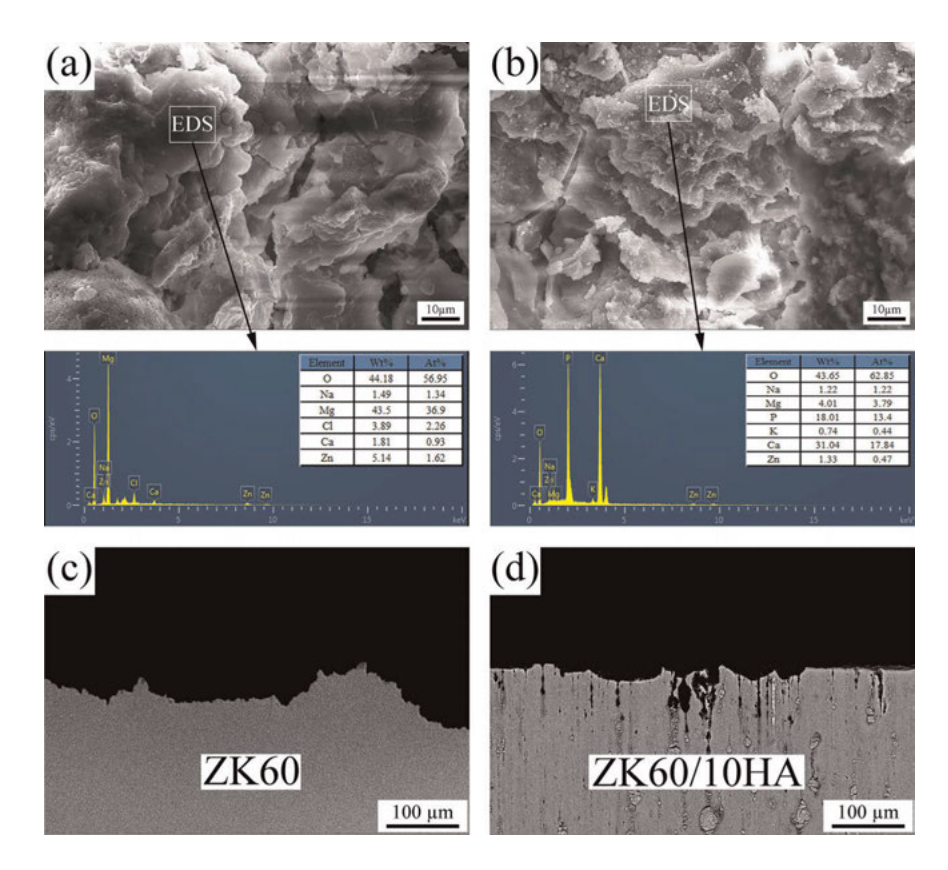


Fig. 7. SEM images and EDS spectra of the corroded surfaces of (a) ZK60 alloy, and (b) ZK60/10HA composite; and SEM images of transverse section of (c) ZK60 alloy, and (d) ZK60/10HA composite after removing the corrosion products.

Mg(OH)₂. As for ZK60/10HA composite, the corrosion products layer contained 62.85 O, 1.22 Na, 3.79 Mg, 13.4 P, 0.44 K, 17.84 Ca, 0.47 Zn elements (at.%). Except for Mg and O, Ca and P were also rich in the surface layer. The ratio of Ca to P was 1.72, close to 1.67, indicating that they were the bone-like apatite [18]. It can be inferred that apatite layer was formed during the immersion test due to the apatite-inducibility of HA particles. Moreover, based on the corrosion rate of ZK60 alloy and ZK60/HA composites, it can be concluded that the apatite layer formed during corrosion provided effective protection over the matrix. As the content of HA increased to 20 wt.%, however, the apatite inducibility of HA particles was overshadowed due to the agglomeration of HA particles, thus, the corrosive resistance was decreased.

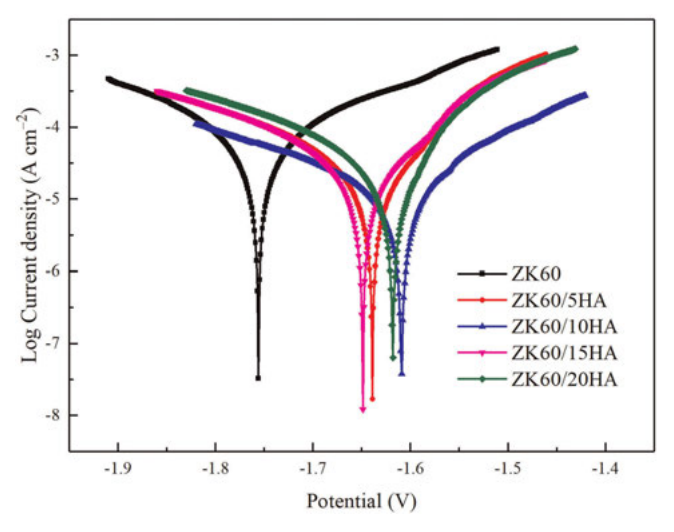


Fig. 8. Electrochemical polarization curves of ZK60 alloy and ZK60/ $\rm HA$ composites.

Table 4. Electrochemical data of ZK60 alloy and ZK60/HA composites.

Samples	$E_{\rm corr}({ m V})$	$I_{\rm corr}$ ($\mu A \ {\rm cm}^{-2}$)
ZK60 ZK60/5HA ZK60/10HA ZK60/15HA ZK60/20HA	-1.76 -1.64 -1.61 -1.65 -1.62	824.5 281.4 258.2 276.3 346.2

Figure 7c and d shows SEM images of the transverse section of ZK60 alloy and ZK60/10HA composite after removing the corrosion products. It appears that the surface of ZK60/10HA composite is much flatter than that of ZK60 alloy, which represents a higher resistance to localized pitting. This can be attributed to the HA induced deposition of apatite on the surface, which inhibited localized corrosion to some extent. In addition, some deeper pits were formed in the subsurface for ZK60/10HA composite, as shown in Fig. 7d. According to the size and morphology of these pits, it can be inferred that it was caused by the peeling off of the HA particles during removing corrosion products. The main reasons for the peeling off of HA particles are the ultrasonic vibration and the severe chemical reaction between Mg(OH)₂ and chromic acid. For ZK60 alloy, the corrosive medium can rapidly invade the interior of the materials along the grain boundaries, which resulted in a high corrosion rate and uneven corrosion surface.

3.5. Electrochemical measurement

The electrochemical polarization curves of ZK60 alloy and ZK60/HA composites are shown in Fig. 8. Each curve can be divided into the anodic polarization section and the cathodic polarization section. The former is attributed to the dissolution of Mg to Mg²⁺, and the latter is related to the hydrogen evolution reaction [32]. The corrosion potential and the corrosion current density calculated by Tafel region extrapolation are listed in Table 4. As shown in Fig. 8 and Table 4, ZK60 alloy exhibited the highest current density and the least positive corrosion potential, which indicated the worst corrosion resistance. In particular, the corrosion current density of ZK60 alloy was 3.2 times that of ZK60/10HA composites.

With the addition of HA, the corrosion current density was decreased when the HA content was lower than $10\,\%$. Further addition of HA led to a slight increase in corrosion current density. Judging by the corrosion current density, the corrosion resistance of materials can be ranked as ZK60/10HA > ZK60/15HA > ZK60/5HA > ZK60/20HA > ZK60, which is completely in agreement with the results of the immersion test.

A schematic model is presented in Fig. 9 to describe HA's effects on the corrosion behavior of ZK60/HA composites. When there were no HA particles, the ZK60 alloy exhibited a uniform corrosion state on a macroscopic scale (Fig. 9a). The surface of the matrix was covered with Mg(OH)₂ during the immersion process. Since Mg(OH)₂ is easily dissolved in the solution containing Cl⁻, it cannot effectively protect the matrix and inhibit further corrosion.

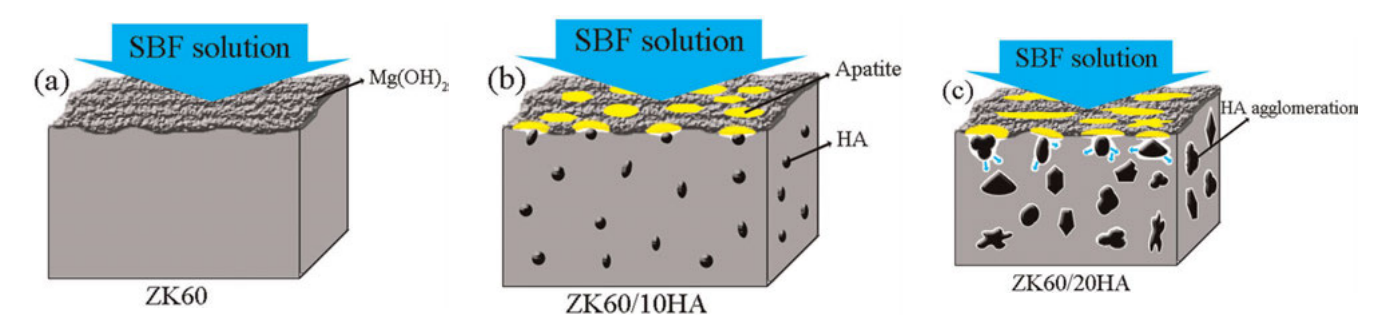


Fig. 9. Schematic diagrams of the corrosion process: (a) ZK60, (b) ZK60/10HA, and (c) ZK60/20HA.

In the case of ZK60/10HA composite, during the corrosion process, the HA can directly contact the SBF solution and induce the formation of apatite, which will not be dissolved by Cl-. The apatite layer covered the surface and can effectively protect the matrix and slow down further corrosion (Fig. 9b), thereby leading to better corrosion re-

However, an excessive HA content can cause the agglomeration of HA and voids at the interface between the matrix and HA, as discussed previously. The SBF solution can readily penetrate into the matrix along the interface and result in further corrosion of the matrix (Fig. 9c). At this point, the apatite-inducibility of HA is not effectively and fully utilized.

4. Conclusions

ZK60-based composites reinforced with HA were fabricated via a powder metallurgy route. The effects of the HA content on microstructure, mechanical properties and in-vitro corrosion behavior of these composites were evaluated. The main conclusions can be drawn as:

- 1. The grains of ZK60/HA composites were refined with the addition of HA. When the HA content reached and exceeded 15 wt.%, the agglomeration of HA particles and voids along the interface between HA and matrix occurred.
- 2. Compared with ZK60 alloy, the addition of HA led to a decrease in compressive strength and hardness of the composite materials to some extent.
- 3. ZK60/10HA composite exhibited a better combination of mechanical strength and corrosion resistance. Compared with ZK60 alloy, the addition of 10 wt.% HA resulted in an increase in corrosion resistance by 38.6%.
- 4. The formation of apatite, induced by HA, covered the surface and can effectively protect the matrix, thereby leading to better corrosion resistance.

The authors acknowledge the financial support of the National Natural Science Foundation of China (Nos. 51574118, 51674118).

References

- [1] S. Nayak, B. Bhushan, R. Jayaganthan, P. Gopinathcd, R.D. Agarwalb, D. Lahiri: J. Mech. Behav. Biomed. Mater. 59 (2016) 57. PMid:26745721; DOI:10.1016/j.jmbbm.2015.12.010
- [2] Song G: Corros. Sci. 49 (2007) 1696. DOI:10.1016/j.corsci.2007.01.001
- [3] Y. Liu, Y. Zheng, X.H. Chen, J.A. Yang, H. Pan, D. Chen, L. Wang, J. Zhang, D. Zhu, S. Wu, K.W.K. Yeung, R.C. Zeng, Y. Han, S. Guan: Adv. Funct. Mater. 29 (2019) 1805402. DOI:10.1002/adfm.201805402 [4] R. Zeng, L. Cui, W. Ke: Acta Metall. Sinica 54 (2018) 1215.
- DOI:10.11900/0412.1961.2018.00032
- [5] D. Xia, Y. Liu, S. Wang, R.C. Zeng, Y. Liu, Y. Zheng, Y. Zhou: Sci. China Mater. 62 (2019) 256. DOI:10.1007/s40843-018-9293-8
- [6] R. Guan, A.F. Cipriano, Z. Zhao, J. Lock, D. Tie, T. Zhao, T. Cui, H. Liu: Mater. Sci. Eng., C 33 (2013) 3661. PMid:23910262; DOI:10.1016/j.msec.2013.04.054

- [7] L.Y. Li, B. Liu, R.C. Zeng, S.Q. Li, F. Zhang, Y.H. Zou, H.G. Jiang, X.B. Chen, S.K. Guan, Q.Y. Liu: Front. Mater. Sci. 12 (2018) 184. DOI:10.1007/s11706-018-0424-1
- [8] L.Y. Cui, X.T. Li, R.C. Zeng, S.Q. Li, E.H. Han, L. Song: Front. Mater. Sci. 11 (2017) 284. DOI:10.1007/s11706-017-0391-y
- [9] M. Moravej, D. Mantovani: Int. J. Mol. Sci. 12 (2011) 4250. PMid:21845076; DOI:10.3390/ijms12074250
- [10] J. Yang, J.L. Guo, A.G. Mikos, C. He, G. Cheng: Ann. Biomed. Eng. 46 (2018) 1229. PMid:29869105; DOI:10.1007/s10439-018-2058-y
- [11] B.R. Sunil, C. Ganapathy, T.S.S. Kumar, U. Chakkingal: J. Mech. Behav. Biomed. Mater. 40 (2014) 178. PMid:25241282; DOI:10.1016/j.jmbbm.2014.08.016
- [12] R.D. Campo, B. Savoini, A. Muñoz, M.A. Monge, G. Garcés: J. Mech. Behav. Biomed. Mater. 39 (2014) 238. PMid:25146678; DOI:10.1016/j.jmbbm.2014.07.014
- [13] F. Witte, F. Feyerabend, P. Maier, J. Fischer, M. Störmer, C. Blawert, W. Dietzel, N. Hort: Biomaterials 28 (2007) 2163. PMid:17276507; DOI:10.1016/j.biomaterials.2006.12.027
- [14] S.S.A. El-Rahman: Pharmacol. Res. 47 (2003) 189. DOI:10.1016/S1043-6618(02)00336-5
- [15] R.C. Zeng, W.C. Qi, H.Z. Cui, F. Zhang, S.Q. Li, E.H. Han: Corros. Sci. 96 (2015) 23. DOI:10.1016/j.corsci.2015.03.018
- [16] A. Feng, Y. Han: Mater. Des. 32 (2011) 2813. DOI:10.1016/j.matdes.2010.12.054
- [17] X. Ye, M. Chen, M. Yang, J. Wei, D. Liu: J. Mater. Sci. Mater. Med. 21 (2010) 1321. DOI:10.1007/s10856-009-3954-3
- [18] C. Shuai, Y. Zhou, Y. Yang, P. Feng, L. Liu, C. He, M. Zhao, S. Yang, C. Gao, P. Wu: Materials 10 (2017) 307. PMid:28772666; DOI:10.3390/ma10030307
- [19] U.C. Gupta, S.C. Gupta: Pedosphere 24 (2014) 13. DOI:10.1016/S1002-0160(13)60077-6
- [20] X. Gu, Y. Zheng, Y. Cheng, S. Zhong, T. Xi: Biomaterials 30 (2009) 484. PMid:19000636; DOI:10.1016/j.biomaterials.2008.10.021
- [21] S. Cai, T. Lei, N. Li, F. Feng: Mater. Sci. Eng. C 32 (2012) 2570. DOI:10.1016/j.msec.2012.07.042
- [22] N.T.C. Oliveira, S.R. Biaggio, R.C. Rocha-Filho, N. Bocchi: J. Biomed. Mater. Res. Part A 74 (2005) 397. PMid:15983989; DOI:10.1002/jbm.a.30352
- [23] G. Song: Adv. Eng. Mater. 7 (2005) 563. DOI:10.1002/adem.200500013
- [24] Y. Chen, Z. Xu, C. Smith, J. Sanker: Acta Biomater. 10 (2014) 4561. DOI:10.1016/j.actbio.2014.07.005
 [25] M.T. Fulmer, I.C. Ison, C.R. Hankermayer, B.R. Constantz,
- J. Ross: Biomaterials 23 (2002) 751. DOI:10.1016/S0142-9612(01)00180-6
- [26] S. Jaiswal, R.M. Kumar, P. Gupta, M. Kumaraswamy, P. Roy, D. Lahiri: J. Mech. Behav. Biomed. Mater. 78 (2018) 442. PMid:29232643; DOI:10.1016/j.jmbbm.2017.11.030
- [27] H.M. Kim, T. Himeno, T. Kokubo, T. Nakamura: Biomaterials 26 (2005) 4366. DOI:10.1016/j.biomaterials.2004.11.022
- [28] T. Kokubo, H. Takadama: Biomaterials 27 (2006) 2907. PMid:16448693; DOI:10.1016/j.biomaterials.2006.01.017
- [29] G. Song, A.L. Bowles, D.H. StJohn: Mater. Sci. Eng. A 366 (2004) 74. DOI:10.1016/j.msea.2003.08.060
- [30] M.P. Staiger, A.M. Pietak, J. Huadmai, G. Dias: Biomaterials 27 (2006) 1728. PMid:16246414; DOI:10.1016/j.biomaterials.2005.10.003
- [31] D. Persaud-Sharma, A. McGoron: J. Biomimetics Biomater. Tissue Eng. 12 (2011) 25. PMid:22408600; DOI:10.4028/www.scientific.net/JBBTE.12.25
- G.L. Song, A. Atrens: Adv. Eng. Mater. 1 (1999) 11. DOI:10.1002/(SICI)1527-2648(199909)1:1<11::AID-ADEM11>3.0.CO;2-N

(Received November 7, 2019; accepted April 22, 2020; online since July 16, 2020)

Correspondence address

Prof. Dr. Jie Teng College of Materials Science and Engineering Hunan University Lushan Road Changsha 410082 P.R. China Tel.: +86-0731-88821727 E-mail: tengjie@hnu.edu.cn Web: www.hnu.edu.cn

Prof. Dr. Zili Xu The first affiliated hospital Hunan Normal University Jiefangxi Road Changsha 410006 P.R. China Tel.: +86-0731-88912416 E-mail: xuzili4848@163.com Web: www.hunnu.edu.cn

Bibliography

DOI 10.3139/146.111930 Int. J. Mater. Res. (formerly Z. Metallkd.) 111 (2020) 8; page 621–631 © Carl Hanser Verlag GmbH & Co. KG ISSN 1862-5282